Geophysical Journal International

Geophys. J. Int. (2018) **214,** 2224–2235
Advance Access publication 2018 June 01
GJI Seismology

doi: 10.1093/gji/ggy201

Directly estimating earthquake rupture area using second moments to reduce the uncertainty in stress drop

Jeffrey J. McGuire[1] and Yoshihiro Kaneko[2]

[1]*Department of Geology and Geophysics, Woods Hole Oceanographic Institution, Woods Hole, MA* 02543, USA. *E-mail: jmcguire@whoi.edu*
[2]*GNS Science,* 1 *Fairway Drive, Avalon, Lower Hutt* 5011, *New Zealand*

Received 2018 May 11; in original form 2018 January 14

SUMMARY

The key kinematic earthquake source parameters: rupture velocity, duration and area, shed light on earthquake dynamics, provide direct constraints on stress drop, and have implications for seismic hazard. However, for moderate and small earthquakes, these parameters are usually poorly constrained due to limitations of the standard analysis methods. Numerical experiments by Kaneko and Shearer demonstrated that standard spectral fitting techniques can lead to roughly one order of magnitude variation in stress-drop estimates that do not reflect the actual rupture properties even for simple crack models. We utilize these models to explore an alternative approach where we estimate the rupture area directly. For the suite of models, the area averaged static stress drop is nearly constant for models with the same underlying friction law, yet corner-frequency-based stress-drop estimates vary by a factor of 5–10 even for noise-free data. Alternatively, we simulated inversions for the rupture area as parametrized by the second moments of the slip distribution. A natural estimate for the rupture area derived from the second moments is $A = \pi L_c W_c$, where L_c and W_c are the characteristic rupture length and width. This definition yields estimates of stress drop that vary by only 10 per cent between the models but are slightly larger than the true area averaged values. We simulate inversions for the second moments for the various models and find that the area can be estimated well when there are at least 15 available measurements of apparent duration at a variety of take-off angles. The improvement compared to azimuthally averaged corner-frequency-based approaches results from the second moments accounting for directivity and removing the assumption of a circular rupture area, both of which bias the standard approach. We also develop a new method that determines the minimum and maximum values of rupture area that are consistent with a particular data set at the 95 per cent confidence level. For the Kaneko and Shearer models with 20+ randomly distributed observations and $\sim$ 10 per cent noise levels, we find that the maximum and minimum bounds on rupture area typically vary by a factor of two and that the minimum stress drop is often more tightly constrained than the maximum.

Key words: Earthquake Dynamics; Earthquake Source Observations; Body Waves.

1 INTRODUCTION

Since the pioneering work of Brune (1970) and Madariaga (1976), seismologists have attempted to map the observable effects of source finiteness for small earthquakes into information about the rupture area and then onto an estimate of the static stress change averaged over the rupture surface (Abercrombie 1995; Ide *et al.* 2003; Prieto *et al.* 2004; Abercrombie & Rice 2005; Shearer *et al.* 2006; Allmann & Shearer 2007, 2009; Yamada *et al.* 2010). Countless studies have reported estimates of static stress drop, $\Delta\sigma$, using expressions derived by Eshelby (1957) for an elliptical crack in a homogeneous elastic medium of the form:

$$\Delta\sigma = C(a, b, \nu)\frac{M_0}{bS}, \tag{1}$$

where M_0 is seismic moment, S the rupture area and C a constant of order unity that depends on the shape of the rupture ellipse with major axis a and minor axis b and the Poisson ratio, ν, of the medium (see also Keilis-Borok 1957). Eq. (1) is somewhat daunting when dealing with real data because it relies on knowing not only the rupture area but also its smallest dimension, in this case the minor axis b. The Brune and Madariaga models avoided this difficulty by having a simple circular rupture patch ($a = b$) resulting in the straightforward connection to the observable average corner frequency $\overline{f_c}$ through the usual expressions:

$$\Delta\sigma = \frac{7}{16}\frac{M_0}{a^3}, \qquad \overline{f_c} = \kappa\frac{\beta}{a} \tag{2}$$

where κ is a constant that is specific to a particular dynamic model. Even if the crack models were an accurate representation of real earthquakes, the stress-drop estimates derived from real data have considerable estimation error because the observable quantity, $\overline{f_c}$ is cubed. Relatively small measurement errors (factor of two) can yield an order of magnitude uncertainty in stress drop. Boatwright (1984a,b) demonstrated that much of the scatter in static stress-drop estimates could be removed for small earthquakes by independently constraining source geometry rather than by applying the Brune formulae, but this has rarely been done in practice for earthquakes smaller than magnitude 6.

We use a suite of 16 dynamic rupture models of simple crack like ruptures from Kaneko & Shearer (2014, 2015) to explore the limits of stress-drop resolution from far-field observables. The models are simple in that they are all crack-like ruptures with uniform initial stress and friction properties, but they illustrate the effects of basic geometrical variations on far-field body waves. Some models have a circular geometry and some are elliptical with a 2:1 aspect ratio. The rupture velocity, stress drop and epicentre location also vary (Fig. 1 and Table 1) to provide a range of kinematic realizations of ruptures with the same length. As a result of the differences in kinematics, the models have different durations (Fig. 2) and corner frequencies (Table 1). Table 1 and Fig. 3 show five estimates of stress drop for each model. Two are calculated directly from the change in shear traction along the fault in the numerical model and are known as the area averaged ($\Delta\sigma_A$) and energy averaged ($\Delta\sigma_E$) stress drops (Noda *et al.* 2013). They represent the actual physical stress drop on the fault surface. Table 1 also shows three ways of estimating stress drop using the far-field body waves. The corner-frequency-derived stress drop for P and S waves ($\Delta\sigma_{f_c^P}$ and $\Delta\sigma_{f_c^S}$) uses eq. (2) with $\overline{f_c}$ averaged over the focal sphere for P and S waves, respectively, and a uniform value of κ as one would do in a typical observational study. These values of $\Delta\sigma_{f_c}$ show the expected factor of eight scatter (Fig. 3) even with perfectly known values of $\overline{f_c}$. In comparison, the estimates derived from the second moments of the rupture (defined later), $\Delta\sigma_2$, are tightly clustered for a given value of the true stress drop. The inherent difficulty in estimating stress drop even for simple crack models using the corner-frequency method in part reflects the variation in rupture duration for the different types of models as well as from the effects of directivity which do not average simply in all cases. The second moment estimates account for these features of the rupture and produce much more consistent estimates regardless of the details of the rupture. The second moment estimates are slightly higher than the area averaged estimates because their weighted average nature characterizes a smaller area than the total rupture area (Fig. 1, Table 1).

2 THEORY: THE SECOND MOMENTS REPRESENTATION AND STRESS DROP

The simplest model-free description of an earthquake rupture that contains information on the width of the slip distribution and hence on the stress drop is the second moments. There is considerable background literature on second moments. In general they describe the overall kinematic properties of a rupture that are well constrained by the far-field waveforms. For a more detailed theoretical background and examples in various settings, see: Backus & Mulcahy (1976a,b); Backus (1977a,b); Doornbos (1982a,b); Silver (1983); Gusev & Pavlov (1988); Bukchin (1995); Das & Kostrov (1997); McGuire *et al.* (2001); Clévédé *et al.* (2004). They have also been used to analyse rupture dynamics simulations (Ampuero & Ben-Zion 2008; Dempsey & Suckale 2016). Here we give a brief introduction with a focus on the quantification of rupture area for a generic slip distribution and the relationship between second moments and the corner frequency of a far-field body wave. For an earthquake with a constant moment tensor such that the spatial variations in moment-rate are described by:

$$\dot{\underline{\underline{M}}}(\underline{r},t) = \underline{\underline{\hat{M}}}\,\dot{f}(\underline{r},t). \tag{3}$$

The second moments are defined as:

$$\begin{aligned}
\hat{\underline{\underline{\mu}}}^{(2,0)} &= \int\int \dot{f}(\underline{r},t)(\underline{r}-\underline{r}_0)(\underline{r}-\underline{r}_0)\mathrm{d}V\mathrm{d}t \\
\hat{\mu}^{(0,2)} &= \int\int \dot{f}(\underline{r},t)(t-t_0)(t-t_0)\mathrm{d}V\mathrm{d}t \\
\hat{\underline{\mu}}^{(1,1)} &= \int\int \dot{f}(\underline{r},t)(\underline{r}-\underline{r}_0)(t-t_0)\mathrm{d}V\mathrm{d}t,
\end{aligned} \tag{4}$$

where $\dot{f}(\underline{r},t)$ is a scalar function that describes the spatial and temporal distribution of moment release (McGuire *et al.* 2001), and $\underline{r}_0$ and t_0 denote the centroid location and time (i.e. the first moments), respectively. The hat denotes that these are central moments taken about the centroid. The integrals are taken over the entire source volume and earthquake duration (Backus 1977a,b; McGuire *et al.* 2001). When $\dot{f}(\underline{r},t)$ is integrated over the volume of the source, it is known as the moment-rate or source time function (STF) $\dot{M}(t)$. The second spatial moment $\hat{\underline{\underline{\mu}}}^{(2,0)}$, is related to the spatial extent of the rupture area, the second temporal moment $\hat{\mu}^{(0,2)}$ is related to the duration of rupture, and the mixed moment $\hat{\underline{\mu}}^{(1,1)}$ is related to rupture propagation.

The characteristic rupture duration τ_c, rupture length L_c and average propagation velocity of the instantaneous spatial centroid $\underline{v}_0$ are defined following Backus & Mulcahy (1976a), Backus (1977a), Silver & Jordan (1983), Silver (1983) and McGuire *et al.* (2001):

$$\begin{aligned}
x_c(\hat{\underline{n}}) &= 2\sqrt{\hat{\underline{n}}^T\,\hat{\underline{\underline{\mu}}}^{(2,0)}\,\hat{\underline{n}}} \\
\tau_c &= 2\sqrt{\hat{\mu}^{(0,2)}} \\
v_c &= L_c/\tau_c \\
\underline{v}_0 &= \hat{\underline{\mu}}^{(1,1)}/\hat{\mu}^{(0,2)},
\end{aligned} \tag{5}$$

where x_c is the spatial extent of the rupture in the direction $\hat{\underline{n}}$ and L_c is the maximum value of x_c (i.e. corresponding to the largest eigenvalue of $\hat{\underline{\underline{\mu}}}^{(2,0)}$). W_c corresponds to the second largest eigenvalue, for example, the rupture width. The second moments can either be calculated in three spatial dimensions (10 unknowns) or along a 2-D fault-plane (six unknowns) if the mechanism is known.

In general the characteristic dimensions give an idea of the region that contributed substantially to moment-release and the relative importance of directivity in the rupture. Fig. 1 shows examples of the characteristic rupture length and width calculated for three of the crack models. For each model, we show two ellipses, one with semimajor/minor axes equal to $L_c/2$ and $W_c/2$ and a larger one with semimajor and minor axes equal to L_c and W_c where the orientation of the ellipse is determined by the eigenvectors of $\hat{\underline{\underline{\mu}}}^{2,0}$. The exact relationship between L_c, W_c and the total rupture dimension depends on the particular slip distribution as they represent weighted averages that are sensitive to the details of the distribution. For the crack models with uniform stress drop, the smaller ellipse captures the region with highest slip, while the larger ellipse approximates the total rupture area (Fig. 1). While the three models in Fig. 1 are characterized by nearly identical stress drops and rupture lengths, their variability is captured by the differences in rupture width W_c, duration τ_c, and directivity $\underline{v}_0$ (Table 1).

The fundamental problems in using the corner-frequency method to estimate stress drop are that it does not estimate W_c and that it

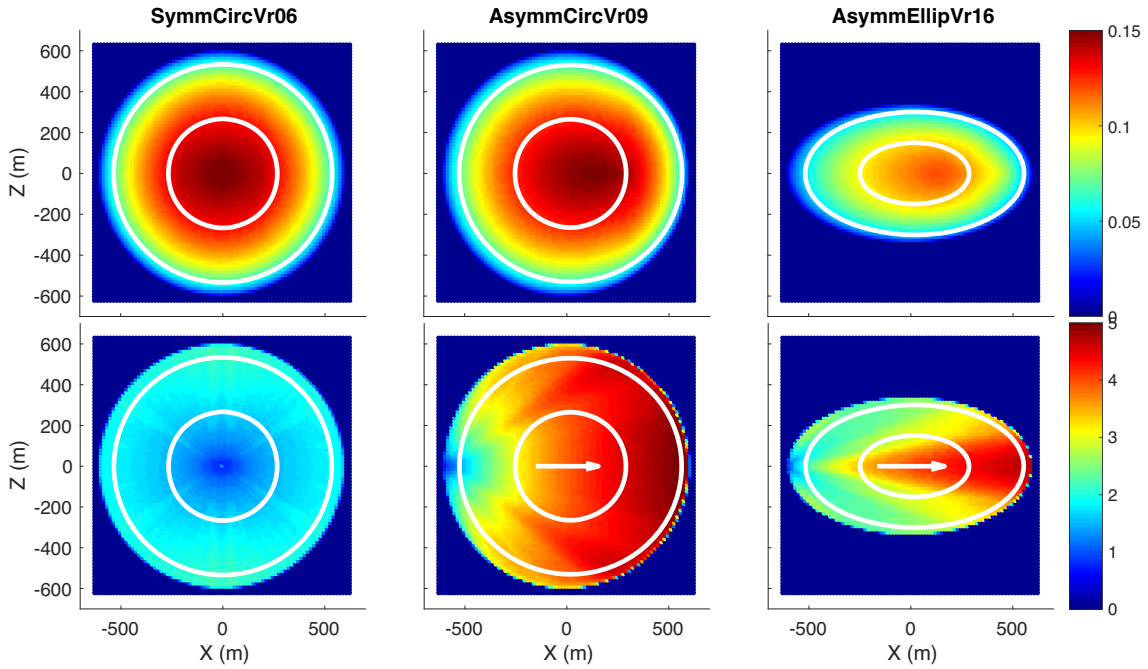

Figure 1. Examples of the slip (top) and peak slip-rate (bottom) distributions for three of the models in Table 1. The slip colourbar is in metres and the slip-rate colourbar is in metres per second. Each panel has two white ellipses. The smaller ellipse has semi-major and semi-minor axes corresponding to $L_c/2$ and $W_c/2$, respectively. The outer ellipse has semi-major and semi-minor axes corresponding to L_c and W_c, respectively. The epicentre for the Symmetric Circular models is in the centre (dark blue slip-rate) while for the Asymmetric Circle and Asymmetric Ellipse models it is on the left-hand edge of the ellipse (dark blue colours in slip-rate). The white arrows have a length and orientation given by the second moments (e.g. $v_0\tau_c$ defined later).

Table 1. The dynamic models of Kaneko & Shearer (2014, 2015) used in this study. $\Delta\sigma_A$, $\Delta\sigma_E$, $\Delta\sigma_{\bar{f}_c^S}$, $\Delta\sigma_{\bar{f}_c^P}$, $\Delta\sigma_2$ and $\Delta\sigma_d$ denote the area averaged stress drop, the energy stress drop, the stress-drop estimate using the average S-wave corner frequency (assuming a constant $\kappa^S = 0.25$), the stress-drop estimate using the average P-wave corner frequency (assuming a constant $\kappa^P = 0.30$), the estimate using the second moments (assuming area $= \pi L_c W_c$), and the prescribed dynamic stress drop, respectively. The seismic moments are in units of 10^{15} Nm. The semi-major axes (e.g. half the rupture length) of all models is 600 m and the semi-minor axis (e.g. half the rupture width) is either 600 m for the circular models or 337 m for the elliptical models. $\alpha = \sqrt{3}\beta = 5.0$ km s^{-1}. The second moment estimates of L_c and W_c are thus slightly smaller than the total dimensions of the rupture. The second moment quantities L_c, W_c, τ_c and v_0 are defined in Section 2.

Model	M_0	L_c (m)	W_c (m)	v_0 (km s^{-1})	τ_c (s)	$\bar{f}_c^S$ (Hz)	$\Delta\sigma_{\bar{f}_c^S}$ (MPa)	$\bar{f}_c^P$ (Hz)	$\Delta\sigma_{\bar{f}_c^P}$ (MPa)	$\Delta\sigma_A$ (MPa)	$\Delta\sigma_E$ (MPa)	$\Delta\sigma_2$ (MPa)	$\Delta\sigma_d$ (MPa)
AsymCirc0.6	2.3	545	531	1.3	0.30	0.96	2.3	1.01	1.6	4.5	4.5	6.1	4.0
SymCirc0.6	2.4	535	534	0.0	0.16	1.20	4.9	1.44	4.9	4.7	4.8	6.9	4.0
SymCirc0.9	2.5	534	531	0.0	0.13	1.25	5.7	1.83	10.2	4.8	5.0	7.2	4.0
AsymCirc0.9	2.4	545	530	1.6	0.21	1.35	6.9	1.40	4.4	4.5	4.6	6.5	4.0
AsymEll0.7	0.93	545	301	1.8	0.25	0.91	0.8	0.91	0.5	4.4	4.5	6.2	4.0
AsymEll0.9	0.97	545	300	2.2	0.20	1.25	2.2	1.20	1.1	4.6	4.7	6.4	4.0
AsymEll1.3	1.0	537	301	2.7	0.15	1.49	3.9	1.68	3.2	4.7	4.8	6.7	4.0
AsymEll1.6	1.0	536	301	2.9	0.13	1.59	4.8	2.02	5.7	4.8	4.9	7.0	4.0
AsymCircVr06σ2	1.1	543	530	1.3	0.30	0.91	1.0	0.96	0.7	2.3	2.3	3.1	2.0
AsymCircVr06σ8	4.7	553	536	1.3	0.30	1.06	6.4	1.25	6.1	9	9	12.0	8.0
AsymEllVr16σ2	0.5	535	300	2.9	0.13	1.59	2.4	2.02	2.9	2.4	2.5	3.5	2.0
AsymEllVr16σ8	2.1	541	306	2.9	0.13	1.59	10.0	2.02	11.9	9.6	9.8	13.8	8.0
AsymEllVr09σ2	0.48	545	299	2.2	0.20	1.25	1.1	1.20	0.6	2.3	2.3	3.2	2.0
AsymEllVr09σ8	2.0	551	305	2.2	0.20	1.25	4.6	1.20	2.4	9.2	9.3	12.8	8.0
SymCirc0.9σ2	1.2	531	530	0.0	0.13	1.25	2.8	1.83	5.1	2.4	2.5	3.6	2.0
SymCirc0.9σ8	5.1	544	535	0.0	0.13	1.25	11.7	1.83	21.1	9.4	9.8	14.0	8.0

incorrectly maps variations in τ_c and $\underline{\mathbf{v}}_0$ into variations in rupture area (Table 1). The first eight models in Table 1 have the same underlying friction law and very similar values of $\Delta\sigma_A$ (4.5–4.8 MPa). However, even for noise-free data, if one uses the values of $\overline{f_c}$ averaged over the focal sphere for S waves and the usual formulae with a constant κ (e.g. eq. 2), the resulting stress drop estimates range over a factor of eight from 0.8 to 6.9 MPa. In contrast when the second moment estimates of L_c and W_c for a particular model are used in the original Eshelby stress drop formulae (e.g. eq.1) with a rupture area given by:

$$S = \pi L_c W_c, \tag{6}$$

(e.g. the larger ellipses in Fig. 1), the estimated stress drop ($\Delta\sigma_2$) for all seven models varies only from 6.2 to 7.2 MPa. The second

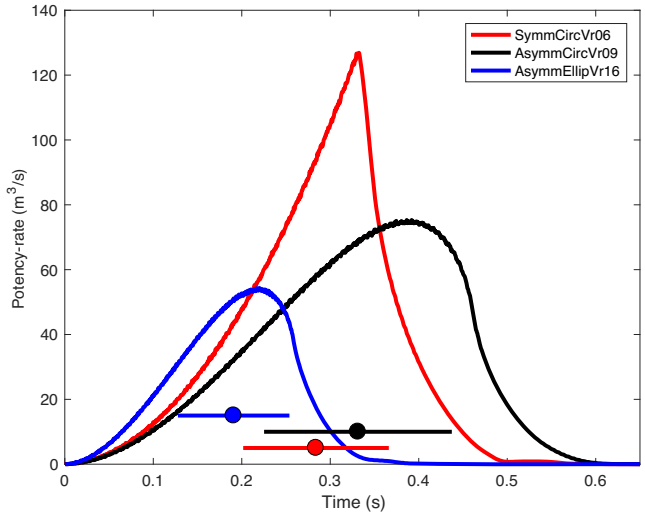

Figure 2. Potency rate functions for the three models is given in Fig. 1. The circles denote the centroid time of each model and the bar through each denotes twice the square root of the variance of the potency rate function (e.g. τ_c defined later) for each model.

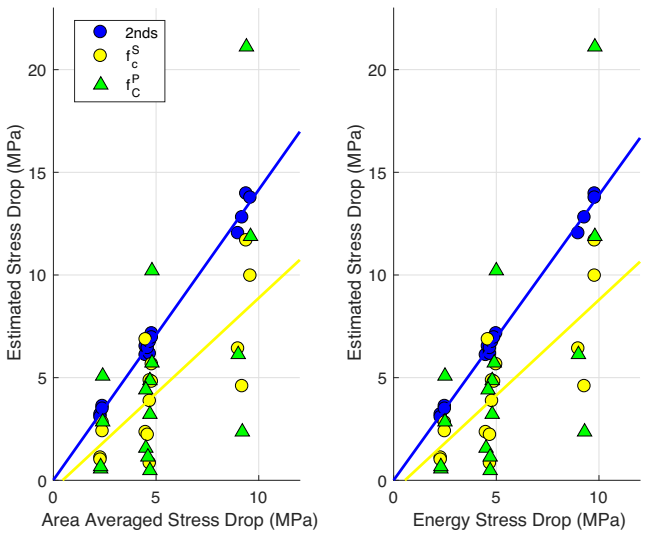

Figure 3. Comparison of stress-drop estimates derived directly from the dynamic models with those derived from the far-field moment-rate functions. All models in Table 1 are plotted. The estimates derived from the second moments are calculated with eq. (1) using $S = \pi L_c W_c$ and $b = W_c$, while the $\overline{f_c}^S$ and $\overline{f_c}^P$ estimates are calculated using eq. (2) with the *S*- or *P*-wave corner frequency averaged over the entire focal sphere (assuming $\kappa^s = 0.25$ and $\kappa^p = 0.30$) following Kaneko & Shearer (2014, 2015). The blue and yellow lines give the best fit to the $\Delta\sigma_2$ and $\Delta\sigma_{\overline{f_c}^S}$ values, respectively.

moment derived estimates are slightly higher than the true area averaged values because this definition of rupture area is slightly smaller than the true area (Fig. 1). However, using an approach based on eqs (1) and (6) would allow an interpretation of stress drop in terms of crack models without the order of magnitude scatter that is inherent in the traditional $\overline{f_c}$ approach (e.g. eq. 2). Fig. 3 shows the effectiveness of the $\Delta\sigma_2$ approach for all of the models in Table 1, which include a range of underlying $\Delta\sigma_A$ values.

2.1 The relationship between f_c and the second moments

Silver (1983) compared the low-frequency amplitude spectrum of the far-field moment-rate function for both the Brune model and a Taylor series expansion based on polynomial moments. For the Brune model, the spectrum is given by:

$$\hat{\Omega}(\hat{\mathbf{r}}, f) = \frac{1}{1 + \left(\frac{f}{f_c}\right)^2}. \tag{7}$$

Silver (1983) and Doornbos (1982a) both showed that a truncated Taylor expansion around zero frequency leads to the equation for the amplitude spectrum

$$\hat{\Omega}(\hat{\mathbf{r}}, f) = 1 - \frac{1}{2} f^2 \mu^{(0,2)}(\underline{s}), \tag{8}$$

where

$$\mu^{(0,2)}(\underline{s}) = \hat{\mu}^{(0,2)} - 2\underline{s} \cdot \underline{\hat{\mu}}^{(1,1)} + \underline{s}^T \cdot \underline{\underline{\hat{\mu}}}^{(2,0)} \cdot \underline{s} \tag{9}$$

denotes the second temporal moment of the STF observed with a particular slowness vector $\underline{s}$ (see Silver (1983) and McGuire (2004) for details). Applying a Taylor expansion to the Brune model and truncating after second order gives an apparent equivalence between the corner frequency and the apparent duration of the far-field moment rate function at a particular slowness:

$$f_c = \sqrt{2} \frac{1}{\sqrt{\mu^{(0,2)}(\underline{s})}}, \tag{10}$$

which is eq. (5) of Silver (1983). Eq. (8) implies an equivalence between measurements of the curvature of the spectrum made in the frequency domain and the duration of the moment-rate function made in the time domain. Eq. (8) is essentially a property of any non-negative function. However, there are multiple approximations involved in reaching eq. (10) due to the truncation of various Taylor series, which particularly for the Brune model limits the validity of (10) to frequencies below the corner frequency. Perhaps more-importantly (10) does not account for how f_c is measured in practice, which involves fitting a two parameter (f_c and n) model to a range of frequencies that extends well above f_c. We find that in practice for the crack models in Table 1 this approximation is not accurate. Silver (1983) found that $\mu^{(0,2)}(\underline{s})$ is more directly related to rupture area than f_c due to the sensitivity of spectral fitting to rapid variations in moment rate. Fig. 4 shows a direct comparison of the two sides of eq. (10) for a distribution of locations on the focal sphere for both *P* and *S* waves. While there is a positive correlation, it is not linear over the whole focal sphere and there is a scale factor of approximately five that is missing between the two sides of eq. (10). In fact, there are fundamental differences in the pattern of azimuthal variations over the focal sphere in f_c and $\mu^{(0,2)}(\underline{s})$ shown in Fig. 5 for one of the unilateral rupture models. There is considerably more structure in the f_c values than in $\tau_c(s) = 2\sqrt{\mu^{(0,2)}(\underline{s})}$. Fig. 5 highlights one of the inherent difficulties in the f_c approach to stress drop. An equally important source of error is that the value of $\overline{f_c}$ determined for a particular data set depends strongly on having full and uniform coverage of the focal sphere. Hence, the variation in the estimates of $\Delta\sigma$ seen in Table 1 are a lower bound that can easily be exceeded with non-ideal sampling of the variations in f_c or simple measurement error of f_c.

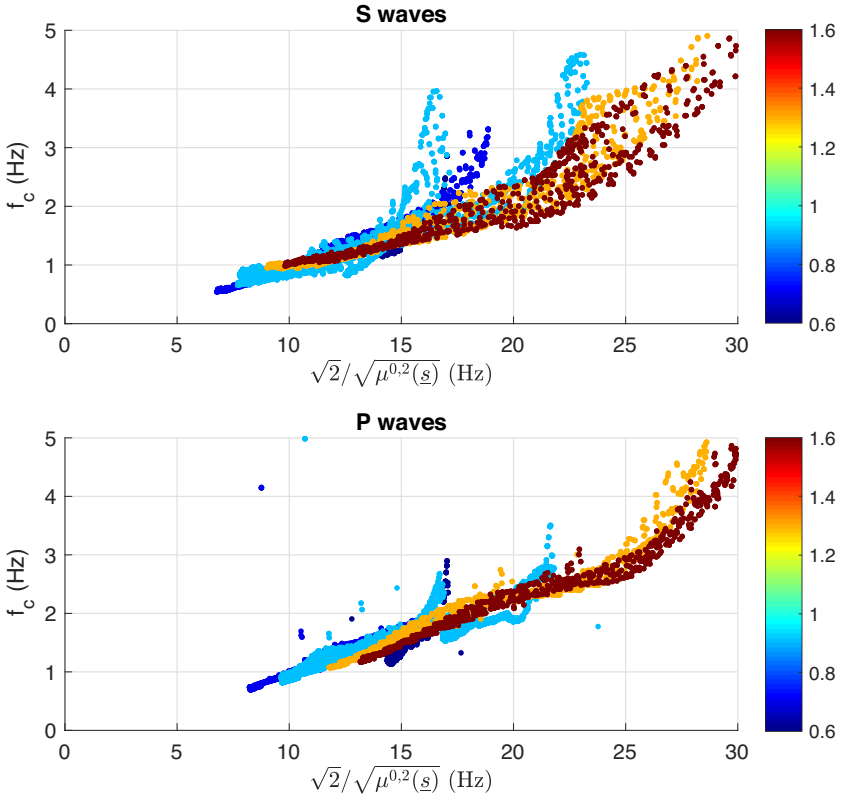

Figure 4. A plot of eq. (10) for the *P* and *S* waves from the first eight dynamic models in Table 1. Each point represents a different location on the focal sphere. The colourbar denotes the ratio of the rupture velocity of the model to the shear wave speed.

3 ESTIMATING THE SECOND MOMENTS

A number of algorithms have been developed to estimate the second moments, and here we follow the approach in McGuire (2004) and McGuire (2017) that utilizes the variations in the observed far-field moment rate functions to set up the inverse problem for the second moments. In general the inverse problem for the second moments can be posed as a simple linear inversion based on eq. (9). However, if the station distribution is suboptimal, this could result in unphysical estimates for the second moments (Das & Kostrov 1997). We enforce the constraint that the source region have non-negative volume (McGuire *et al.* 2001) which is accomplished by enforcing the matrix inequality:

$$\begin{bmatrix} \hat{\underline{\underline{\mu}}}^{(2,0)} & \hat{\underline{\mu}}^{(1,1)^{\mathrm{T}}} \\ \hat{\underline{\mu}}^{(1,1)} & \hat{\mu}^{(0,2)} \end{bmatrix} \geq 0, \tag{11}$$

where ≥ 0 indicates that the matrix is required to be positive semi-definite. Because of this physical constraint, estimating the second moments is most easily done with convex optimization algorithms that can enforce matrix inequality constraints (Vandenberghe & Boyd 1996).

Given a vector of measurements $\underline{b}$, consisting of $\mu^{(0,2)}(\underline{s})$ values at different stations and phases, that are linearly related to a vector $\underline{x}$ containing the six independent elements of the second moments, eq. (9) becomes $\underline{\underline{A}}\underline{x} = \underline{b}$. Finding the best estimate of the second moments involves solving the least-squares problem for $\underline{x}$ subject to eq. (11). To take advantage of convex optimization techniques, the problem is stated as a linear objective function and a set of Linear Matrix Inequalities (LMI) given by:

$$\begin{aligned} &\text{minimize} \quad \mathrm{c} \\ &\text{subject to} \quad \begin{bmatrix} c & (\underline{\underline{A}}\underline{x} - \underline{b})^{\mathrm{T}} \\ \underline{\underline{A}}\underline{x} - \underline{b} & \underline{\underline{I}}^{N} \end{bmatrix} \geq 0\,, \\ &\text{and} \quad \begin{bmatrix} \hat{\underline{\underline{\mu}}}^{(2,0)} & \hat{\underline{\mu}}^{(1,1)^{\mathrm{T}}} \\ \hat{\underline{\mu}}^{(1,1)} & \hat{\mu}^{(0,2)} \end{bmatrix} \geq 0\,, \\ &\text{and} \quad \hat{\mu}^{(0,2)} \leq \max(\mathrm{b}) \end{aligned} \tag{12}$$

where $\underline{\underline{I}}^{N}$ is the identity matrix with dimension equal to the number of measurements, N (McGuire 2017). The equivalence between the linear least-squares problem and the above can be seen by calculating the eigenvalues of the $N + 1$ by $N + 1$ matrix, which are non-negative when the matrix is positive semi-definite. This restatement of the problem is known as using Schur complements to represent a nonlinear constraint as LMI (Vandenberghe & Boyd 1996). The last equation ensures that the estimate of the second temporal moment is smaller than the largest measurement of $\mu^{(0,2)}(\underline{s})$, which should be true for any data set that contains stations with good azimuthal coverage.

The LMI system in eq. (12) thus gives the optimal estimate of L_c and W_c and hence rupture area. Figs 6 and 7 show results of inversions using this scheme for two of the dynamic rupture models. In each example, a number of synthetic data sets were generated by randomly sampling the focal sphere for *P* and *S*-wave measurements of $\mu^{(0,2)}(\underline{s})$ and adding Gaussian noise proportional to the true duration of the model rupture ($N(0,\ 0.1\tau_c)$). Figs 6 and 7 show the inversion results as a function of the number of observations in each synthetic data set. For data sets as small as

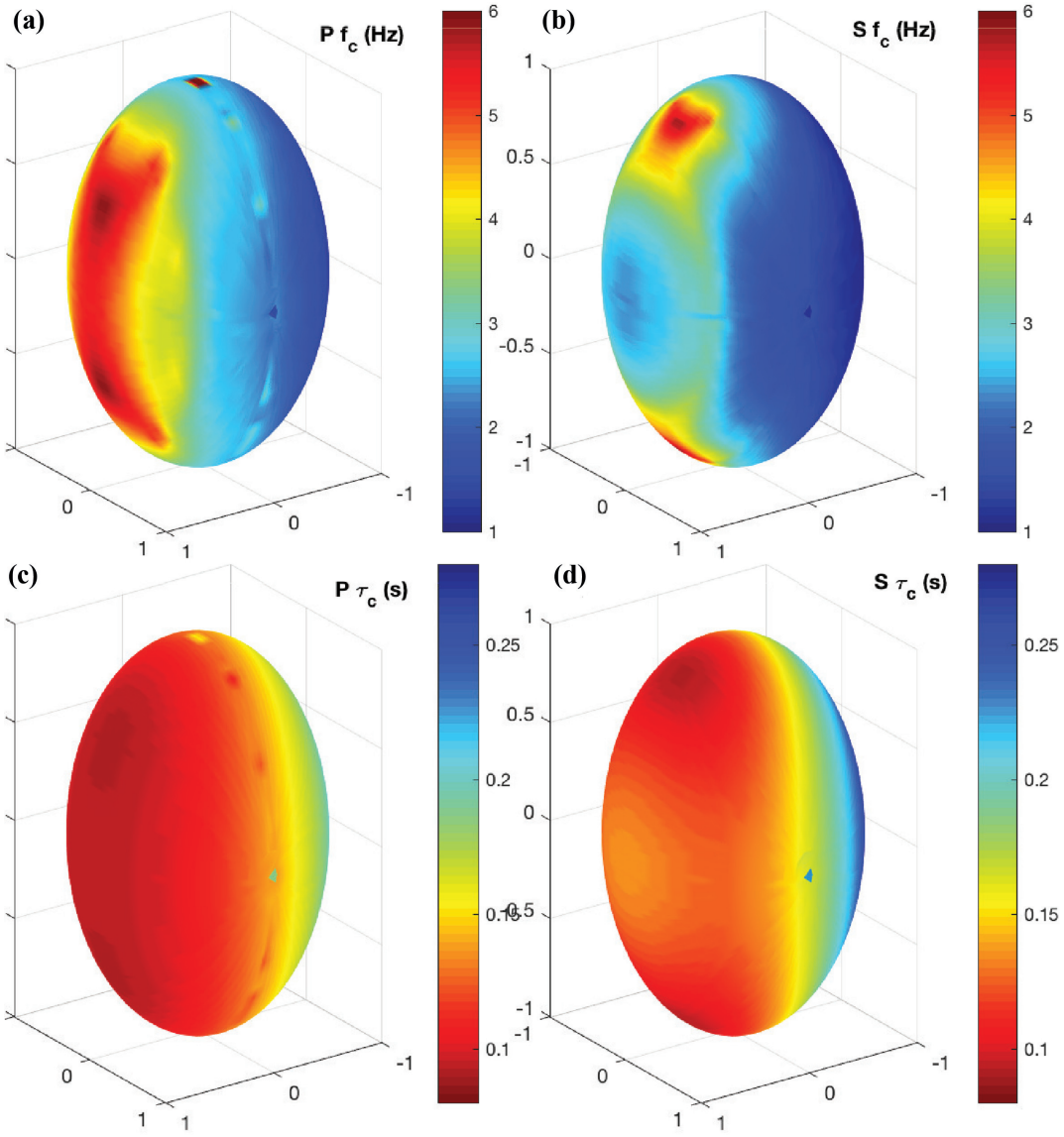

Figure 5. Variations in corner frequency (f_c) and apparent duration ($\tau_c(\underline{s})$) over the focal sphere for AsymmEllip1.6. The corner-frequency colourbars are in Hertz and the apparent duration colourbars are in seconds.

15 observations, there is considerable scatter around the true values that results from incomplete coverage of the focal sphere. Data sets with about 30 or more measurements have a very good recovery of the true values. Of particular interest for the stress-drop problem is the ability to differentiate the values of W_c and area between Figs 6 and 7. For data sets with $N \geq 30$, the W_c estimates in Fig. 7 are significantly smaller than those in Fig. 6 as one would expect from the models (Fig. 1). This more accurate representation of rupture area is what allows the $\Delta\sigma_2$ estimates to be more accurate than the $\Delta\sigma_{f_c}$ estimates of stress drop.

4 DETERMINING UPPER AND LOWER BOUNDS ON RUPTURE AREA

To evaluate the uncertainty in rupture area, and hence stress drop, we use a new approach that seeks to determine the upper and lower bounds on rupture area that are permissible for a given data set. Studies using second moments have often used approaches such Jackknife and Bootstrap techniques to evaluate the uncertainties in the characteristic rupture quantities (McGuire 2017). For determining maximum and minimum bounds on rupture area, this is not an ideal approach because of the trade-offs between the elements of $\underline{x}$. Here we develop a new approach based on χ^2 confidence bounds. The definition of the χ^2 statistic:

$$\chi^2 = \sum_i^N \frac{(b_i - \hat{b}_i)^2}{\sigma_i^2} \tag{13}$$

requires knowledge of the measurement uncertainty σ_i. In practice, say for the Empirical Green's Function (EGF) approach in McGuire (2017), this uncertainty is not well known. We use the standard assumption that the misfit to the data set for the optimal estimate of the second moments corresponds to a reasonable estimate of the average value of $\sigma = \sigma_i$ and that it is constant among all measurements. Some observational studies are starting to use multiple EGF events on the same main shock as a way to estimate the uncertainties at an individual station. Given this estimate of σ and the number

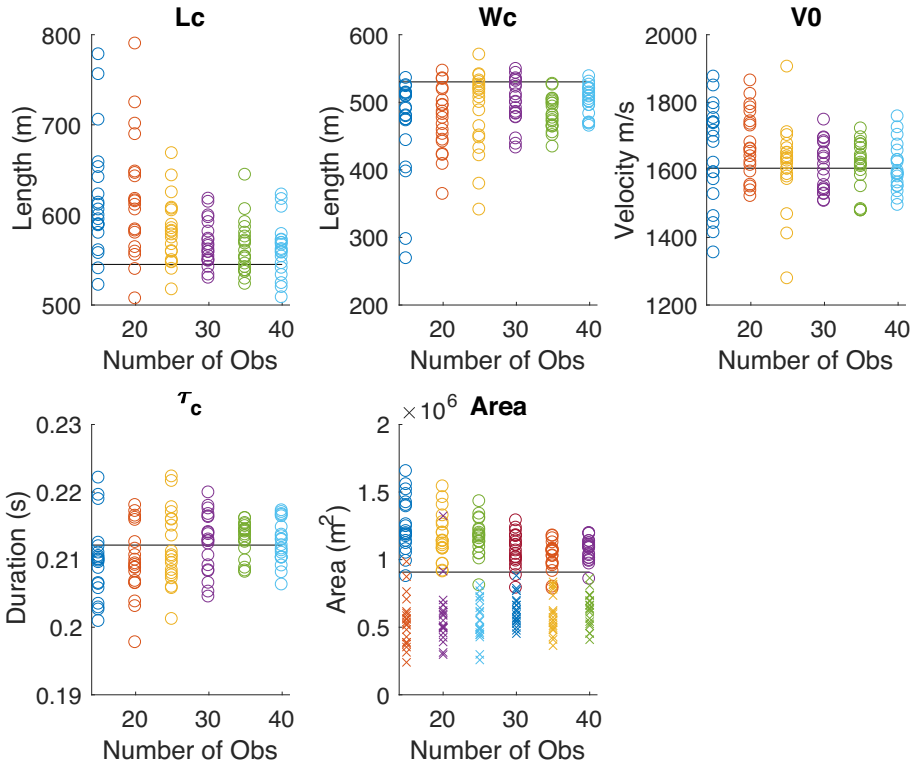

Figure 6. Inversion results from synthetic data sets for model AsymmCirc0.9 The solid lines give the true value of each quantity. Each circle represents and individual inversion result from a synthetic data set of randomly distributed *P* and *S* waves with the total number of observations in the data set as the *x*-axis. For the Area plot, circles represent the upper bound and *x*'s represent the lower bound at 95 per cent confidence.

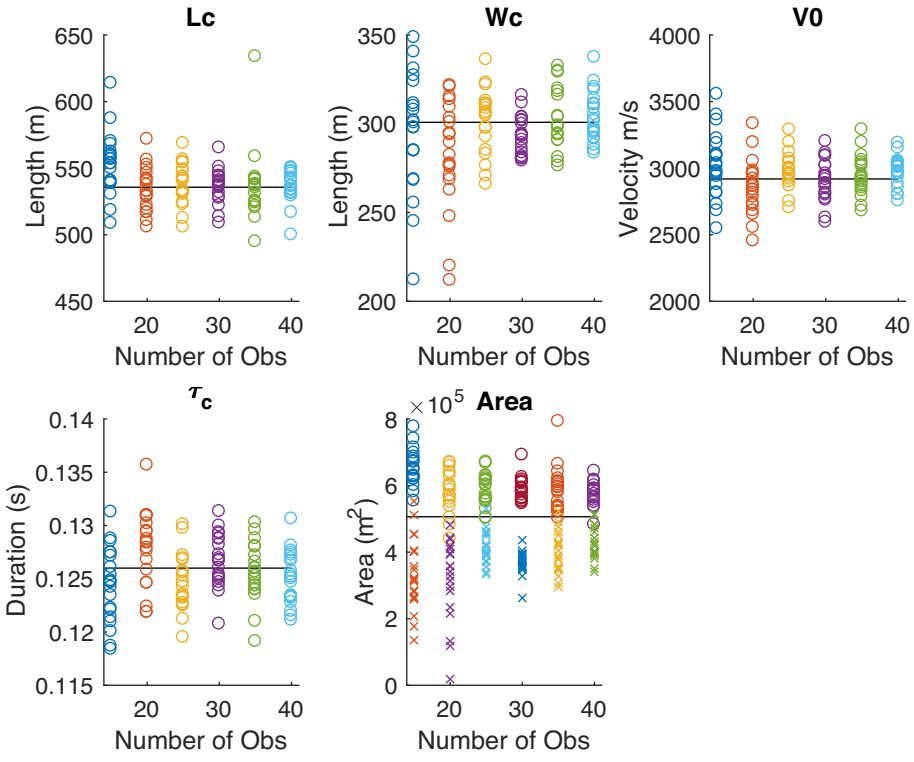

Figure 7. Inversion results from synthetic data sets for model AsymmEll1.6. The solid lines give the true value of each quantity.

of degrees of freedom in the estimation problem, we utilize tables of χ^2 values to specify the misfit that would correspond to a given confidence level. We then determine the minimum or maximum rupture area that is consistent with the chosen confidence level.

To determine the maximum rupture area using convex optimization, we solve a determinant maximization problem (Vandenberghe & Boyd 1996)

$$\begin{aligned} &\text{maximize} \quad \left| \underline{\underline{\mu}}^{(2,0)} \right| \\ &\text{subject to} \quad \begin{bmatrix} \sigma^2 \chi_c^2 & (\underline{\underline{A}}\underline{x} - \underline{b})^{\mathrm{T}} \\ \underline{\underline{A}}\underline{x} - \underline{b} & \underline{\underline{I}}^N \end{bmatrix} \geq 0 \\ &\text{and} \quad \begin{bmatrix} \hat{\underline{\underline{\mu}}}^{(2,0)} & \hat{\underline{\mu}}^{(1,1)^{\mathrm{T}}} \\ \hat{\underline{\mu}}^{(1,1)} & \hat{\mu}^{(0,2)} \end{bmatrix} \geq 0\,, \\ &\text{and} \quad \hat{\mu}^{(0,2)} \leq \max(\mathrm{b}) \end{aligned} \tag{14}$$

where χ_c^2 denotes the value of χ^2 for a particular confidence level c. Solving (14) provides a upper bound on rupture area and hence a lower bound on stress drop. The problem specified by eq. (14) is convex and hence can be solved by a variety of algorithms. Unfortunately, the opposite problem, namely to minimize $L_{\mathrm{c}}W_{\mathrm{c}}$ is not convex and hence is not a tractable approach to determining an upper bound on $\Delta\sigma$. This is also true for simply trying to minimize W_{c}. However, there are a number of related problems which are convex and allow the allowable range of rupture areas to be investigated. All of the following are convex problems that can be easily solved:

(i) minimize L_{c}.
(ii) maximize W_{c}.
(iii) minimize $L_{\mathrm{c}}^2 + W_{\mathrm{c}}^2$.
(iv) maximize $L_{\mathrm{c}}^2 + W_{\mathrm{c}}^2$.
(v) maximize L_{c}.

To approximate a lower bound on rupture area, we solve the problem:

$$\begin{aligned} &\text{minimize} \quad \mathrm{L}_{\mathrm{c}}^2 + \mathrm{W}_{\mathrm{c}}^2 \\ &\text{subject to} \quad \begin{bmatrix} \sigma^2 \chi_c^2 & (\underline{\underline{A}}\underline{x} - \underline{b})^{\mathrm{T}} \\ \underline{\underline{A}}\underline{x} - \underline{b} & \underline{\underline{I}}^N \end{bmatrix} \geq 0 \\ &\text{and} \quad \begin{bmatrix} \hat{\underline{\underline{\mu}}}^{(2,0)} & \hat{\underline{\mu}}^{(1,1)^{\mathrm{T}}} \\ \hat{\underline{\mu}}^{(1,1)} & \hat{\mu}^{(0,2)} \end{bmatrix} \geq 0\,, \\ &\text{and} \quad \hat{\mu}^{(0,2)} \leq \max(\mathrm{b}) \end{aligned} \tag{15}$$

While this is not a precise lower bound on S that one would like to use in eq. (1), it provides a rough estimate of the minimum rupture area at a given confidence level. For both the minimum and maximum area inversions we used CVX, a Matlab package for specifying and solving convex programs (Grant and Boyd, 2008, 2014).

We demonstrate the bounds from solving eqs (14) and (15) for the Asymmetric Circular and Asymmetric Ellipse models in Figs 8 and 9 which have very similar values of $\Delta\sigma_2$ using the true values of L_{c} and W_{c} (6.5 and 7.0 MPa, respectively) despite having rupture widths that vary by almost a factor of two. For data sets with $N \geq 25$, the upper and lower 95 per cent confidence bounds are within a factor of two and the optimal estimate approximates the true value. Even with realistic noise added and imperfect station coverage, the range in permissible stress-drop values for $\Delta\sigma_2$ is only a factor of 2. This is substantially less than the factor of 8 variation in the optimal

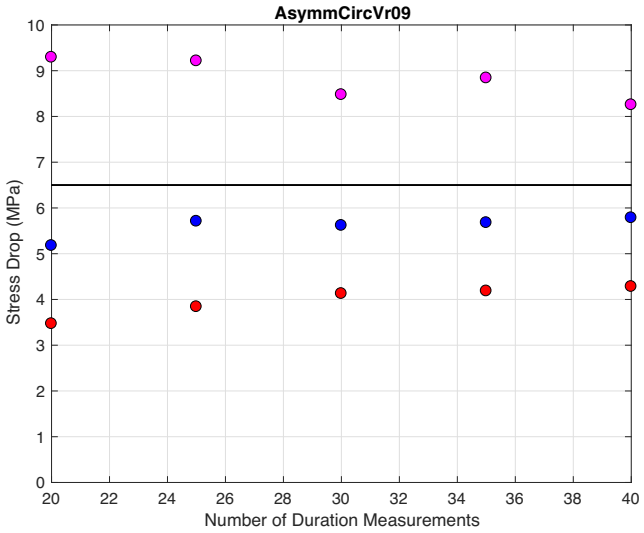

Figure 8. The best-fit (blue), minimum rupture area (cyan) and maximum rupture area (red) inversion results for the AsymmCirc 0.9β model. Each point shows the average of 150 realizations of the synthetic data set made by randomly choosing stations and assigning them to be P or S waves and adding Gaussian noise ($N(0,0.1\tau_{\mathrm{c}})$) to the apparent duration measurements. The optimization problems in eqs (13) and (14) were solved assuming $N_{\mathrm{df}} = N - 3$.

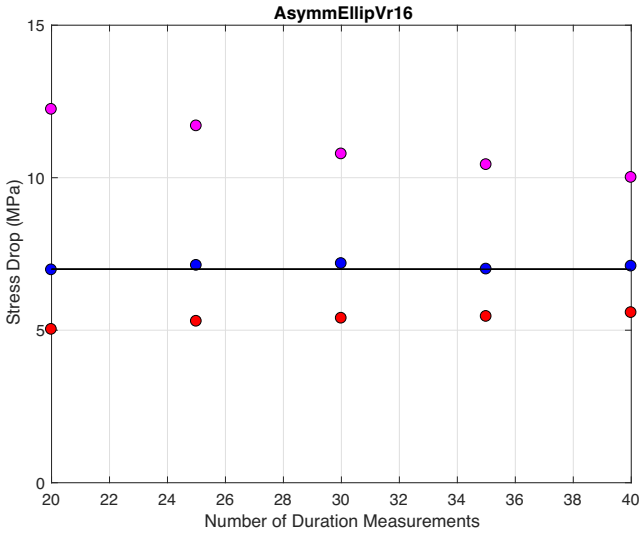

Figure 9. The same as Fig. 8 but for the ASymmEll 1.6β model

estimate that is inherent in the f_{c} method even when using perfect data and perfect averaging over the whole focal sphere (Table 1).

4.1 Appropriate choice of the number of degrees of freedom

One subtle aspect of the method presented in eqs (13) and (14) is the specification of the number of degrees of freedom in the estimation problem. For the 2-D fault case a simple answer would be that $N_{\mathrm{df}} = N - 6$ because of the six independent elements of the second moments on a 2-D fault. This turns out to be an underestimate because the additional LMIs in eqs (13) and (14) (e.g. the non-negative volume constraint) effectively reduce the dimension of the model space. Fig. 10 shows the results from 10 000 synthetic

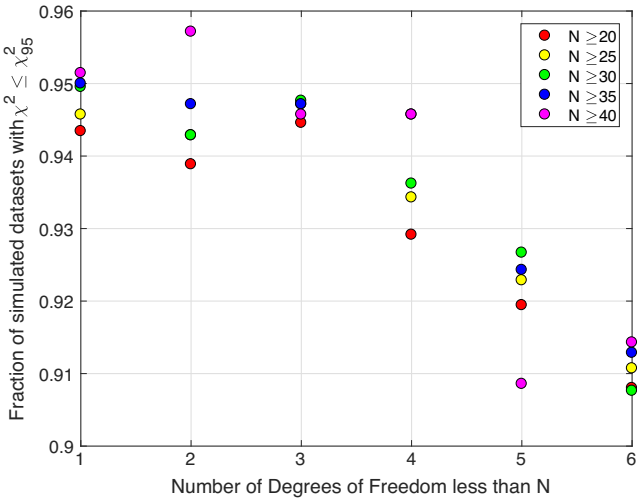

Figure 10. The fraction of synthetic data sets that have misfits less than the expected 95 per cent confidence level compared to the assumed number of degrees of freedom.

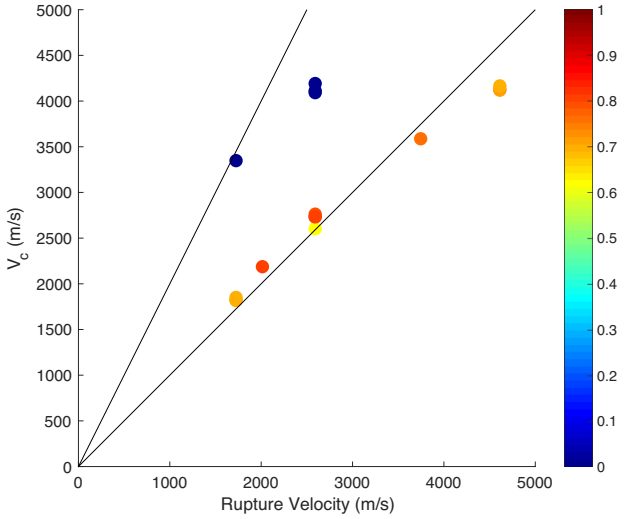

Figure 11. Comparison of the prescribed rupture velocity in the model versus the value of V_c from the model's second moments. Lines with a slope of 1 and 2 show the expected values for perfectly unilateral and bilateral ruptures respectively. Each of the 16 models is shown with a circle colour coded by its value of the directivity ratio $(|\underline{v}_0| * \tau_c)/L_c$. The shear wave speed in the models is 2887 m s^{-1}.

data sets derived from the first seven models in Table 1. For each data set, synthetic noise was added similar to Figs 8 and 9 and the best estimate of the second moments was determined. The fraction of best-fit models with a misfit less than the 95 per cent confidence limit is shown compared to the assumed N_{df} for various possible values (e.g. $N_{df} = N - 1$, $N_{df} = N - 2$, ...). We find that the appropriate choice of $N_{df} = N - 3$ is the largest value that accurately reproduces the misfit statistics. This value was used in Figs 8 and 9. Hence, the LMIs in eqs (13) and (14) have the effect of reducing the dimension of the model space by about 3. This points out the advantageous features of using the second moments for estimating stress drop. Despite being a general representation that can be utilized with eq. (1), they have a limited number of free parameters and allow for specific tests on the upper and lower bounds of possible rupture areas.

5 PLACING FAR FIELD CONSTRAINTS ON RUPTURE VELOCITY

An equally interesting quantity to estimate for rupture dynamics is the velocity with which the rupture front propagates across the fault, V_r. V_r is inherently difficult to resolve with far-field data because of the intermixing of rupture geometry and rise time in controlling the P and S wave pulse shapes. The second moments are related to V_r, but not in a unique way. For a uniform slip rupture with instantaneous rise time, they are directly related in the case of an exactly bilateral rupture ($V_c = L_c/\tau_c = 2V_r$) or a perfectly unilateral rupture ($|\underline{v}_0| = V_r$) (McGuire *et al.* 2002). Even simple crack models like those used here deviate from these ideal cases, but since the 16 models in Table 1 are either nearly perfectly bilateral or unilateral they approximate these relationships as shown in Fig. 11. These relationships place two lower bounds on V_r for an arbitrary slip distribution.

$$\begin{aligned} V_r &\geq |\underline{v}_0| \\ V_r &\geq \tfrac{1}{2}\tfrac{L_c}{\tau_c}. \end{aligned} \tag{16}$$

Owing to the weighted average nature of the second moments and the inherent uncertainties in estimating them with typical data sets, these inequalities likely would not identify events where only a fraction of the rupture may have been super-shear. However, Fig. 11 indicates that estimating the second moments is a plausible way to constrain V_r for smooth unilateral ruptures.

One potential use of applying the second moment method to small earthquakes would be to identify portions of major faults that produce supershear ruptures and correlate that with fault-zone geology as has been done for large earthquakes and in numerical models (e.g. Robinson *et al.* 2010; Bruhat & Dunham 2016). Kaneko & Shearer (2014, 2015) point out that for supershear ruptures such as in Fig. 5, there are rapid variations in the far-field S-wave pulse shape near the forward rupture direction. In general, the measurements of $\mu^{(0,2)}(\underline{s})$ vary more smoothly over the focal sphere than those of f_c or n even for the supershear case (Fig. 5). Figs 12 and 13 compare how the measurable quantities $\tau_c(\underline{s})$, f_c, and n change in the forward and backward direction between a subshear ($V_r = 0.9\beta$) and super-shear ($V_r = 1.3\beta$) case that are otherwise identical. In both cases $\tau_c(\underline{s})$ measurements vary smoothly for both P and S waves and the change in V_r is manifest as a change in the minimum and maximum values of $\tau_c(\underline{s})$. In contrast, the values of f_c and n derived from spectral fitting show much more rapid variations due to the rapid variations in pulse shape near the forward direction (Figs 12 and 13). The f_c variations can be somewhat reduced by calculating f_c as the peak of the far-field S-wave velocity spectrum that has been smoothed to reduce the influence of rupture velocity (Figs 12 and 13).

After Brune's initial paper, there was considerable debate about the relationship between P- and S-wave corner frequencies and which should be expected to be higher (Savage 1972; Molnar *et al.* 1973; Dahlen 1974; Savage 1974; Hanks 1981). Silver (1983) showed that in general, $\tau_c(\underline{s}) = 2\sqrt{\mu^{(0,2)}(\underline{s})}$, should be longer for S waves than P waves as a basic consequence of source kinematics and that their ratio should not be used to differentiate between dynamic models. Figs 12 and 13 indicate that the ratio of $\tau_c(\underline{s})$ for the P wave to $\tau_c(\underline{s})$ for the S wave might be a powerful way to identify supershear ruptures. This ratio is significantly lower (~0.75) in the forward direction for the supershear case than the subshear case (~1.1). Stated another way, for the supershear case, the stations with the shortest source time functions (smallest $\tau_c(\underline{s})$) should

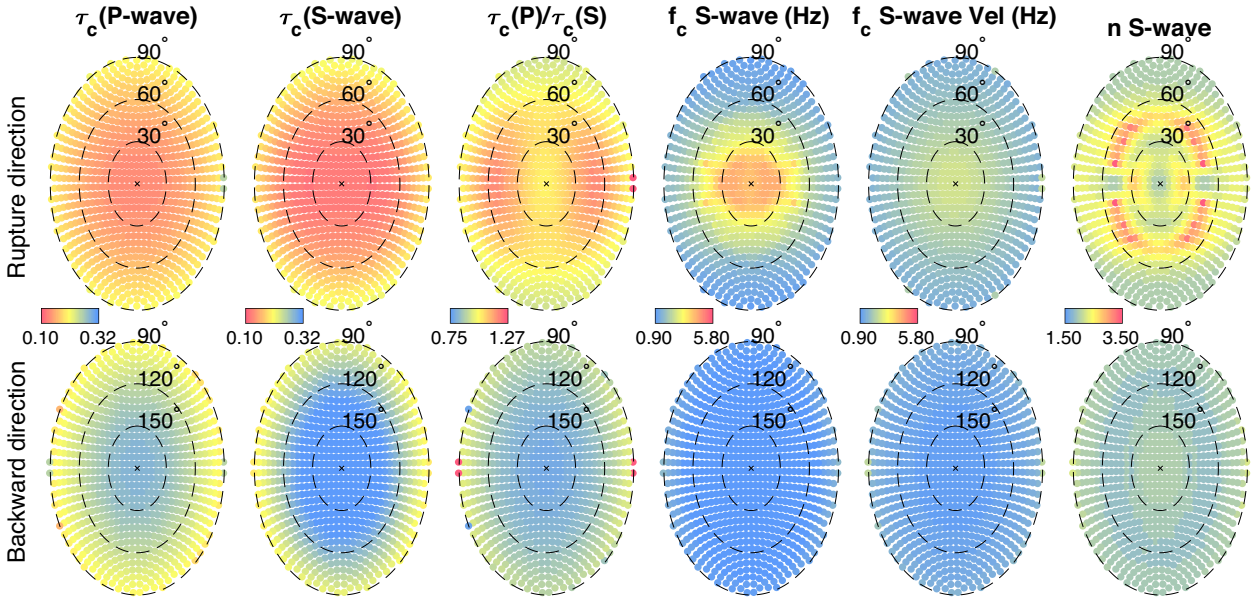

Figure 12. Variations of $\tau_c(\underline{s}) = 2\sqrt{\mu^{(0,2)}(\underline{s})}$ for the P and S waves over the focal sphere, and the ratio of those two quantities for the Asymmetric Elliptical rupture models with $V_r = 0.9\beta$. Also shown are the values of f_c for the S wave calculated from spectral fitting and calculated as the peak of the smoothed velocity spectrum, and the fall-off exponent n derived from spectral fitting. The rupture direction is at the origin (0°) and the backward direction is at 180°.

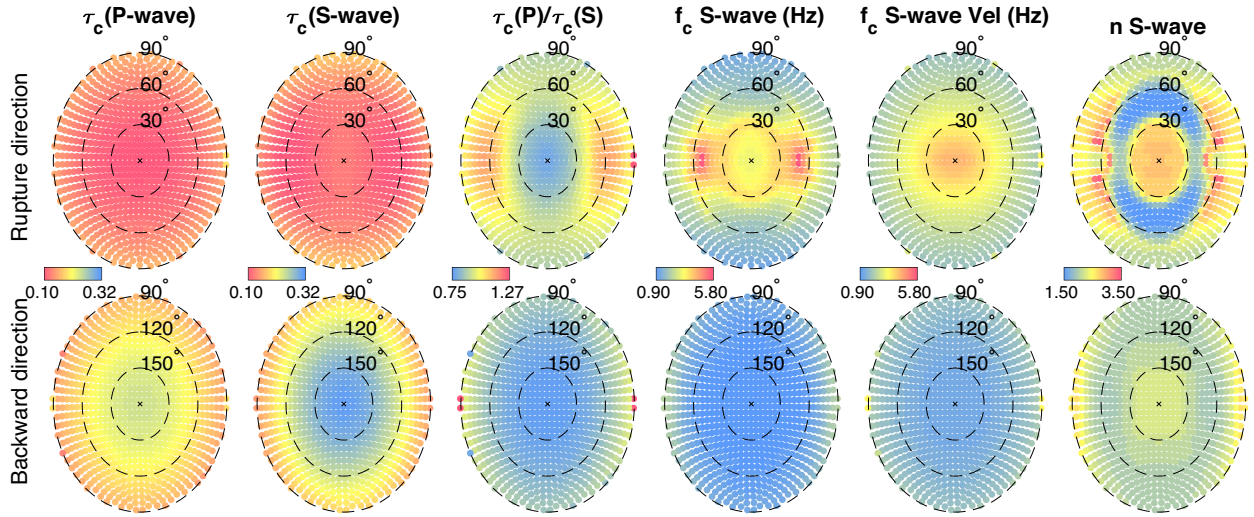

Figure 13. Variations of $\tau_c(\underline{s}) = 2 * \sqrt{\mu^{(0,2)}(\underline{s})}$ for the P and S waves over the focal sphere, and the ratio of those two quantities for the asymmetric elliptical rupture models with $V_r = 1.3\beta$. Also shown are the values of f_c for the S wave calculated from spectral fitting and calculated as the peak of the smoothed velocity spectrum, and the fall-off exponent n derived from spectral fitting.

have values of this ratio that are significantly less than 1.0. This suggests a supershear diagnostic that does not require any inversion for the second moments or the fitting of a spectral model to high frequencies. Fig. 14 shows the variation of this ratio for each of the three models in Fig. 1 as a function of the apparent duration of the S wave. For the circular models, there is a simple decrease in this ratio, $\tau_c(\underline{s})$ (P wave)/$\tau_c(\underline{s})$(S wave), with increasing $\tau_c(\underline{s})$ (S wave). For the unilateral, but subshear ruptures this general trend exists albeit with some small variations. However, for the unilateral, supershear case there is a clear separation of the points into a second regime in the forward direction that has extremely small values of this ratio (∼0.7) (Fig.14). Similar plots for all 16 models in Table 1 show that only the supershear cases show the type of distribution seen in the right-hand panel of Fig. 14 with very low values of $\tau_c(\underline{s})$ (P wave)/$\tau_c(\underline{s})$ (S wave) at the shortest measured values of $\tau_c(\underline{s})$. As Fig. 14 is simply a plot of measurements, this could be a powerful, model-free, diagnostic for identifying supershear ruptures.

6 CONCLUSIONS

Seismological studies of static stress drop for small and moderate earthquakes have been plagued with multiple orders of magnitude of estimation uncertainty for decades. The vast majority of these studies have relied on eq. (2) or slightly modified forms of the corner-frequency model. As Fig. 3 shows, the simplifying assumptions in this approach produce about 1 order of magnitude in scatter even for perfect measurements on ideal crack-like ruptures. Given the difficulty in estimating f_c from real data sets, the non-crack complexities of real ruptures and the f_c^3 term in eq. (2), it is clear that

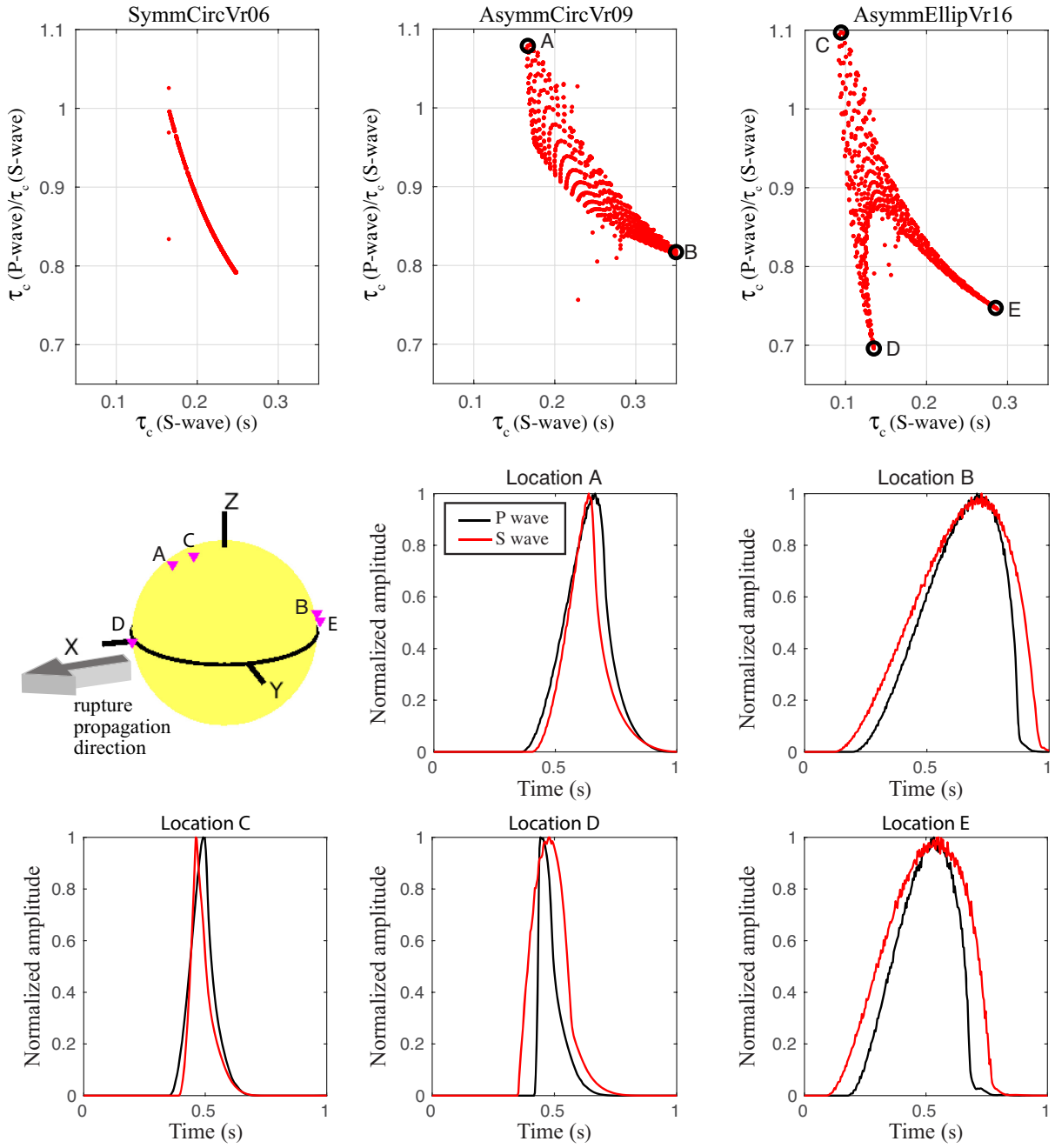

Figure 14. Comparison of the ratio of $\tau_c(\underline{s})$ (*P* wave)/$\tau_c(\underline{s})$(*S* wave) for three different models in Table 1 and Fig. 1. The top three panels show all points covering the entire focal sphere. The location of representative receivers (A–E) on the focal sphere and the magnitude of farfield *P* (in black) and *S* wave (in red) displacements at these receivers are also shown. The black circle on the *x*–*y* plane is parallel to the fault surface. The hypocentre is located in the receiver B and E side.

much of the observational scatter is due to the basic properties of the method rather than true earthquake variations. We have proposed a different approach for estimating stress drop that is based on the original (more general) eqs (1) and (6), and the second moments inversion scheme. This approach eliminates much of the scatter produced by over simplified models of the source (Fig. 3). We have also developed extensions to the second moment inversion method that specifically determine the 95 per cent confidence bounds on rupture area for a given data set and hence provide upper and lower bounds on stress drop in addition to the optimal value. We find that for the crack models, the upper and lower bounds are often asymmetric with the lower bound being tighter than the upper bound due to the inherent difficulty in ruling out small values of rupture width. With the next generation recording systems for microearthquakes that enable dense sampling of the wavefield, as well as ever better regional networks, modern data sets are now sufficient to implement this approach and constrain rupture area to a factor of two or better for moderate earthquakes (Fan & McGuire 2018). The second moment method also provides lower bound constraints on rupture velocity that can prove useful, particularly for unilateral ruptures. We have also identified a measurement scheme that may be particularly useful in identifying supershear ruptures. We suggest that given the dense station distributions of many modern earthquake data sets, a shift towards using the second moment method might

greatly improve the usefulness of seismic studies of moderate earthquake stress drops in terms of reflecting real variations in fault-zone properties rather than estimation errors.

ACKNOWLEDGEMENTS

This work was supported by USGS NEHRP Award G17AP00029. Thanks to Wenyuan Fan for help with the figures. We thank Peter Shearer for providing his code to estimate the peak of the smoothed velocity spectrum. The research was supported by the Southern California Earthquake Center (SCEC; Contribution No. 8013). SCEC is funded by NSF Cooperative Agreement EAR-1033462 and USGS Cooperative Agreement G12AC20038. YK was supported by both public funding from the Government of New Zealand and the Royal Society of New Zealand's Rutherford Discovery Fellowship. We thank editor M. Mai and two anonymous reviewers for thorough reviews and helpful suggestions.

REFERENCES

Abercrombie, R.E., 1995. Earthquake source scaling relationships from -1 to 5 ml using seismograms recorded at 2.5-km depth, *J. geophys. Res,* **100**(B12), 24 015–24 036.

Abercrombie, R.E. & Rice, J.R., 2005. Can observations of earthquake scaling onstrain slip weakening? *Geophys. J. Int,* **162**(2), 406–424.

Allmann, B.P. & Shearer, P.M., 2007. Spatial and temporal stress drop variations in small earthquakes near parkfield, california, *J. geophys. Res.,* **112**(B4), B04305.

Allmann, B.P. & Shearer, P.M., 2009. Global variations of stress drop for moderate to large earthquakes, *J. geophys. Res.,* **114,** 22.

Ampuero, J.P. & Ben-Zion, Y., 2008. Cracks, pulses and macroscopic asymmetry of dynamic rupture on a bimaterial interface with velocity-weakening friction, *Geophys. J. Int.,* **173**(2), 674–692.

Backus, G. & Mulcahy, M., 1976a. Moment tensors and other phenomenological descriptions of seismic sources. 2. discontinuous displacements, *Geophys. J. R. astr. Soc.,* **47**(2), 301–329.

Backus, G. & Mulcahy, M., 1976b. Moment tensors and other phenomenological descriptions of seismic sources—continuous displacements, *Geophys. J. R. astr. Soc.,* **46**(2), 341–361.

Backus, G.E., 1977a. Interpreting seismic glut moments of total degree 2 or less, *Geophys. J. R. astr. Soc.,* **51**(1), 1–25.

Backus, G.E., 1977b. Seismic sources with observable glut moments of spatial degree 2, *Geophys. J. R. astr. Soc.,* **51**(1), 27–45.

Boatwright, J., 1984a. The effect of rupture complexity on estimates of source size, *J. geophys. Res.,* **89,** 1132–1146.

Boatwright, J., 1984b. Seismic estimates of stress release, *J. geophys. Res.,* **89,** 6961–6968.

Bruhat, L.F.Z. & Dunham, E.M., 2016. Rupture complexity and the supershear transition on rough faults, *J. geophys. Res.,* **121**.

Brune, J.N., 1970. Tectonic stress and the spectra of seismic shear waves from earthquakes, *J. geophys. Res.,* **75,** 4997–5009.

Bukchin, B.G., 1995. Determination of stress glut moments of total degree-2 from teleseismic surface-wave amplitude spectra, *Tectonophysics,* **248**(3-4), 185–191.

Clévédé, E., Bouin, M.-P., Bukchin, B., Mostinskiy, A. & Patau, G., 2004. New constraints on the rupture process of the 1999 August 17 Izmit earthquake deduced from estimates of stress glut rate moments, *Geophys. J. Int.,* **159**(3), 931–942.

Dahlen, F.A., 1974. On the ratio of p-wave to s-wave corner frequencies for shallow earthquake sources, *Bull. seism. Soc. Am.,* **64,** 1159–1180.

Das, S. & Kostrov, B.V., 1997. Determination of the polynomial moments of the seismic moment rate density distribution with positivity constraints, *Geophys. J. Int.,* **131**(1), 115–126.

Dempsey, D. & Suckale, J., 2016. Collective properties of injection-induced earthquake sequences: 1. model description and directivity bias, *J. geophys. Res.,* **121**(5).

Doornbos, D.J., 1982a. Seismic moment tensors and kinematic source parameters, *Geophys. J. R. astr. Soc.,* **69**(1), 235–251.

Doornbos, D.J., 1982b. Seismic source spectra and moment tensors, *Phys. Earth planet. Inter.,* **30**(2-3), 214–227.

Eshelby, J.D., 1957. The determination of the elastic field of an ellipsoidal inclusion, and related problems, *Proc. R. Soc.,* **241**(1226), 376–396.

Fan, W. & McGuire, J.J., 2018. Investigating microearthquake finite source attributes with the iris community wavefield demonstration experiment in oklahoma, *Geophys. J. Int.,* **214,** 2, 1072–1087, in press.

Gusev, A.A. & Pavlov, V.M., 1988. Determination of space-time structure of a deep earthquake source by means of power moments, *Tectonophysics,* **152**(3-4), 319–334.

Hanks, T.C., 1981. The corner frequency shift, earthquake source models, and q, *Bull. seism. Soc. Am.,* **71,** 597–612.

Ide, S., Beroza, G.C., Prejean, S.G. & Ellsworth, W.L., 2003. Apparent break in earthquake scaling due to path and site effects on deep borehole recordings, *J. geophys. Res.,* **108**(B5),

Kaneko, Y. & Shearer, P., 2014. Seismic source spectra and estimated stress drop derived from cohesive-zone models of circular subshear rupture, *Geophys. J. Int.,* **197,** 1002–1015.

Kaneko, Y. & Shearer, P.M., 2015. Variability of seismic source spectra, estimated stress drop, and radiated energy, derived from cohesive-zone models of symmetrical and asymmetrical circular and elliptical ruptures, *J. geophys. Res.,* **120**(2).

Keilis-Borok, V.I., 1957. On the estimation of the displacement in an earthquake source and of source dimensions, *Ann. Geofis.,* **12,** 205–214.

Madariaga, R., 1976. Dynamics of an expanding circular fault, *Bull. seism. Soc. Am.,* **66,** 639–666.

McGuire, J.J., 2004. Estimating finite source properties of small earthquake ruptures, *Bull. seism. Soc. Am.,* **94**(2), 377–393.

McGuire, J.J., 2017. A matlab toolbox for estimating the second moments of earthquake ruptures, *Seismol. Res. Lett.,* **88**(2A), 371–378.

McGuire, J.J., Zhao, L. & Jordan, T.H., 2001. Teleseismic inversion for the second-degree moments of earthquake space-time distributions, *Geophys. J. Int.,* **145**(3), 661–678.

McGuire, J.J., Zhao, L. & Jordan, T.H., 2002. Predominance of unilateral rupture for a global catalog of large earthquakes, *Bull. seism. Soc. Am.,* **92**(8), 3309–3317.

Molnar, P., Tucker, B.E. & Brune, J.N., 1973. Corner frequencies of p and s waves and models of earthquake sources, *Bull. seism. Soc. Am.,* **63,** 2091–2104.

Noda, H., Lapusta, N. & Kanamori, H., 2013. Comparison of average stress drop measures for ruptures with heterogeneous stress change and implications for earthquake physics, *Geophys. J. Int.,* **193**(2), 1691–1712.

Prieto, G.A., Shearer, P.M., Vernon, F.L. & Kilb, D., 2004. Earthquake source scaling and self-similarity estimation from stacking p and s spectra, *J. geophys. Res.,* **109**(B8), B08310.

Robinson, D.P., Das, S. & Searle, M.P., 2010. Earthquake fault superhighways, *Tectonophysics,* **493,** 236–243.

Savage, J.C., 1972. Relation of corner frequency to fault dimensions, *J. geophys. Res.,* **77,** 3788–3795.

Savage, J.C., 1974. Relation between p- and s-wave corner frequencies in the seismic spectrum, *Bull. seism. Soc. Am.,* **64,** 1621–1627.

Shearer, P.M., Prieto, G.A. & Hauksson, E., 2006. Comprehensive analysis of earthquake source spectra in southern california, *J. geophys. Res.,* **111**(B6), B06303.

Silver, P., 1983. Retrieval of source-extent parameters and the interpretation of corner frequency, *Bull. seism. Soc. Am.,* **73**(6), 1499–1511.

Silver, P.G. & Jordan, T.H., 1983. Total moment spectra of 14 large earthquakes, *J. geophys. Res.,* **88**(NB4), 3273–3293.

Vandenberghe, L. & Boyd, S., 1996. Semidefinite programming, *SIAM Rev.,* **38**(1), 49–95.

Yamada, T., Okubo, P.G. & Wolfe, C.J., 2010. Kiholo bay, Hawai'i, earthquake sequence of 2006: relationship of the main shock slip with locations and source parameters of aftershocks, *J. geophys. Res.,* **115**.